



City Research Online

City, University of London Institutional Repository

Citation: Kyriazis, N., Koukouvinis, F. & Gavaises, E. (2019). Numerical investigations on bubble-induced jetting and shock wave focusing: application on a needle-free injection. *Proceedings of the Royal Society A*, 475(2222), 20180548. doi: 10.1098/rspa.2018.0548

This is the accepted version of the paper.

This version of the publication may differ from the final published version.

Permanent repository link: <https://openaccess.city.ac.uk/id/eprint/21632/>

Link to published version: <https://doi.org/10.1098/rspa.2018.0548>

Copyright: City Research Online aims to make research outputs of City, University of London available to a wider audience. Copyright and Moral Rights remain with the author(s) and/or copyright holders. URLs from City Research Online may be freely distributed and linked to.

Reuse: Copies of full items can be used for personal research or study, educational, or not-for-profit purposes without prior permission or charge. Provided that the authors, title and full bibliographic details are credited, a hyperlink and/or URL is given for the original metadata page and the content is not changed in any way.

City Research Online:

<http://openaccess.city.ac.uk/>

publications@city.ac.uk

Numerical investigations on bubble-induced jetting and shock wave focusing: application on a needle-free injection

Nikolaos Kyriazis¹, Phoevos Koukouvini¹ and Manolis Gavaises¹

Abstract

The formation of a liquid jet into air induced by the growth of a laser-generated bubble inside a needle-free device is numerically investigated by employing the compressible Navier-Stokes equations. The three co-existing phases (liquid, vapour and air) are assumed to be in thermal equilibrium. A transport equation for the gas mass fraction is solved in order to simulate the non-condensable gas. The homogeneous equilibrium model (HEM) is utilized in order to account for the phase-change process between liquid and vapour. Thermodynamic closure for all three phases is achieved by a barotropic Equation of State (EoS). 2-D axisymmetric simulations are performed for a needle-free device for which experimental data are available and utilised for the validation of the developed model. The influence of the initial bubble pressure and the meniscus geometry on the jet velocity is examined by two different sets of studies. Based on the latter, a new meniscus design similar to shaped-charge jets is proposed, which offers a more focused and higher velocity jet compared to the conventional shape of the hemispherical gas-liquid interface. Preliminary calculations show that the developed jet can penetrate the skin and thus, such configurations can contribute towards a new needle-free design.

1 Introduction

Needle-free injection systems (NFIS) have gained popularity and are widely used nowadays instead of the conventional drug delivery systems, since they offer several benefits, for instance effectiveness in mass immunization programmes. Exposed to infectious diseases, such as HIV and hepatitis, is a great number of workers in the health sector because of accidental needle-stick injuries [1, 2]. Compared to conventional needle injection systems, NFIS can inject not only liquid drugs and vaccines, but also in solid particle form [3] while they ensure faster drug delivery. In addition, self administration with NFIS is feasible, while they usually eliminate pain [4, 5, 3], bleeding or bruising [5, 6], as well as needle-phobia facilitating their use by patients with chronic diseases [6, 1].

Based on the type of load, NFIS can be classified as powder, liquid and projectile injections [7, 6, 3]. NFIS can be also categorized based on the actuation mechanism, with spring and compressed gas being the most common power sources among commercial needle free injection systems (see for example SUMAVEL DosePro by Zogenix [8]). In the present study, a liquid injection system is simulated where the jet is created due to the expansion of a laser-induced bubble [9]. Such laser powered systems are not yet available for clinical use and were originally designed by Yoh et al. [10, 11, 12, 13]. The expansion of the high pressure

bubble results in the creation of a shock wave travelling inside the liquid, which is later reflected by the walls. When the superposition of the waves reaches the liquid-gas interface, a liquid jet is formed in the nozzle which impacts on the skin surface [5, 10, 14]. The objective is to generate a liquid jet strong enough to punch a hole into the skin through erosion and fracture and to deliver the medicine/vaccine into the tissues, without damaging the skin and the drug molecule [6, 3]. After that, the depth of the hole is increased due to further impingement of the jet; the mechanism is the same for all liquid injections. If the volumetric rate of the hole formation is less than the volumetric rate of the jet impinging the skin, backflow is noticed [1, 6]. This splashing back of the liquid from the skin onto the nozzle was responsible for subject-to-subject contamination of hepatitis B virus [15, 5, 1]. Once the jet impacts on the skin, the jet velocity reduces but it continues to travel through the hole, until it reaches a point where the velocity is no longer sufficient to puncture the hole (stagnation point). Because of the dispersion of the jet when it impacts the stagnation point, the hole takes a spherical-like shape [1, 5].

The importance of the contact angle, between the interface and the horizontal wall, on the jet formation has been previously noticed [16, 17, 18] and can be the determining factor on whether the jet will penetrate the skin or not. Apart from NFIS, the same principle is followed in shaped-charge jets, where a hollow cavity with the explosive is lined with a thin layer of metal [19, 16, 20]. The most widely used shaped-charge liner geometries are the conical [21], the hemispherical [22], the trumpet [23] and the bell-shape [24]. Furthermore, the shape of the liner affects the penetration velocity and consequently the depth, as well as the diameter of the hole [19, 24]. For example, conical liner produces deep penetration, whereas the hole diameter is small. On the other hand, hemispherical and bell-shaped liners are used in order to achieve larger diameter holes and shallow penetration. The aforementioned interface geometries have been also utilised for the needle-free injection simulations.

Several works regarding theoretical, experimental and numerical works on liquid jets formed by a shock wave have been performed. Apart from fundamental studies, there are applications in medicine (NFIS), or even in military (shape-charges).

Among the first theoretical studies on the impact of liquid jets on solid boundaries and the fracture which is caused are the works of Benjamin, Ellis [25] and Field [26], whereas Plesset and Chapman [27] simulated the jet produced from a collapsing bubble. Later on, Longuet-Higgins [28] studied axisymmetric jets which were produced by a gas bubble. Since such jets are inertia driven in their initial stage, he modelled them by a Dirichlet hyperboloid, neglecting surface tension and gravity (see also [29]). In a similar work, Antkowiak et al. [16] examined the role of the free-surface geometry on the evolution of the jet, when a tube filled with liquid falls under gravity, by deriving an analytical expression for the velocity field. Furthermore, Katz [20] modelled the aspherical collapse of a bubble and predicted the shape and the velocity of the jet, whereas Sun et al. [30], studied theoretically and experimentally the growth and the collapse of a vapour bubble inside a micro-tube and they demonstrated the role of the thermal effects.

Leighton et al. [31, 32, 33, 34] studied theoretically and experimentally the collapse of a conical gas bubble at the end of a tube filled with liquid. This work was the basis towards the design of needle-free devices and it was later extended by Symons [35], who derived an equation of motion for the liquid displacement. In addition, Bergmann et al. [36] denoted the

importance of the inward radial flow in the strength and formation of the jet on the free surface. A pressurised air filled tube inside a container filled with water was used in their apparatus. After a sudden release of the pressure in the tube, a singularity was formed on the interface. Tagawa et al. [18] produced thin supersonic microjets by vaporisation of liquid in an open capillary. They examined how several parameters such as the contact angle, the distance between the laser focus and the free surface and the diameter of the capillary affect the jet velocity (see also [37], [38], [39]). Later, Hayasaka et al. [9] investigated the effect of the shock wave on the jet velocity and on the cavitation onset. They demonstrated that the jet velocity depends on the pressure impulse of the shock wave and that the probability of cavitation onset depends only on the peak pressure of the shock wave (see also [2]). In a similar device, Avila et al. [40] demonstrated the creation of two different jets, due to the expansion and the collapse of a hemispherical vapour bubble and they reported the potential of such devices in biomedical applications such as NFIS (see also [41]). Finally, Kiyama et al. [42] studied the formation of jet on the gas-liquid interface in a test tube which is induced by gravitational acceleration and hits the rigid floor and they manifested three different types of jet (normal, splashing, cavitating).

Apart from theoretical and experimental studies, several numerical works exist on the topic. Ory et al. [43] studied the growth and the collapse of a vapour bubble in a narrow tube by employing the incompressible Navier-Stokes equations without phase-change (see also [44]). Free surface and surface tension were modelled using the marker-chain technique, where the free surface was described by massless particles (markers). In a similar work, López-Villa et al. [45] simulated the formation of a gaseous bubble inside a tube by a constant gas flow rate and compared their findings against experimental data. By changing the shape of the surrounding walls from cylindrical to conical, they demonstrated that the shape and the volume of the bubbles was also affected. Duchemin et al. [46] simulated a bubble burst at a free surface of liquid and the jet formation with a droplet at its tip. The marker-chain technique has been used there as well for taking into account the free surface and surface tension. In order to satisfy the boundary condition of zero tangential stress on the free surface, a least-square approach has been utilized (see also [47]). Turangan et al. [48] employed a free-Lagrangian method (FLM) for the compressible Euler equations in order to simulate the jetting collapse of air bubbles in the water. They performed simulations for a shock-induced collapse of an initially stable bubble with applications in lithotripsy, as well as for a bubble collapse due to pressure difference between the liquid and the gas (see also [49]). In a follow-up study, Turangan et al. [50] studied shock-induced collapse and its interaction with elastic-plastic material. Finally, Peters et al. [17] simulated cavitating microjets by using a boundary integral code. They elucidated the effect of several parameters on the jet velocity magnitude and they compared their results with the experimental findings of Tagawa et al. [18]. Regarding numerical works in shaped-charge and blast waves, the interested reader is referred to [24, 51, 52].

In the above numerical works, the compressibility effects were neglected, apart from [48]. On the contrary, the compressible Navier-Stokes equations have been modelled in the present study aiming to capture the waves created by the compressed gas and its reflection at the meniscus. To author's best knowledge, in the aforementioned numerical works, either the gas phase (air) or the vapour phase were neglected (except for [47], where only the vapour phase was modelled) and phase change was not modelled. However, in the present study, a 2-phase solver able to model the liquid jet (water), the gas (air) and the cavitation regime in the

nozzle (vapour), has been employed. The minimum Weber number in the present simulations is calculated to be around $We=80$ and thus, surface tension has been neglected. The maximum Reynolds number is around $Re=1410$ and consequently, the flow has been considered to be laminar. Both non-dimensional numbers are based on the jet diameter. It is also worth to mention that the vapour bubble which is created by the focused laser [9, 18], is modelled as a hemisphere of non-condensable gas. The main focus is to study the formation of the primary jet, which is created due to the bursting gas, and to identify the appropriate conditions under which the jet is able to penetrate the skin surface. The vapour bubble collapse and the secondary jet which is created, are out of scope here. The vapour generation due to the laser pulse is a rather complex process to model, as plasma phase is formed [38, 9], several chemical reactions take place and the validity of the existing mass-transfer mechanisms is questionable upon these conditions. Although the penetration into the human skin is not modelled here, erosion and fracture of the skin is estimated based on the velocity of liquid jet. While in previous studies efforts to correlate the dependence of the jet velocity on the contact angle have been made [17, 18], in the present work different meniscus geometries have been investigated.

The paper is organized as follows. In section 2 the numerical method is briefly described. In section 3 the results are demonstrated, including comparison with experimental data. Then, a parametric study of a bubble with initial pressure p_{bub} utilising 2-D axisymmetric simulations is performed, followed by investigation of the flow field for different meniscus geometries while p_{bub} is kept constant. These simulations aim to correlate the micro-jet velocity with the initial bubble pressure and the geometry of the liquid-air interface in the capillary. The most important conclusions are summarised in section 4. In Appendix 5, validation of the numerical method is presented and in Appendix 6, the effect of surface tension is examined in the simulations.

2 Numerical Method

A two-phase solver able to predict phase-change between liquid and vapour, as well as gaseous phase co-existence under equilibrium conditions has been developed in OpenFOAM [53] and has been extensively described and validated in Appendix 5 and [54]. In the present work, the algorithm will be briefly discussed. The three dimensional compressible Navier-Stokes equations in conservative form are considered:

$$\frac{\partial U}{\partial t} + \frac{\partial F_k(U)}{\partial x_k} = 0, \quad \text{in } \Omega, \quad (1)$$

where $k=1,2,3$ denotes summation in the x,y,z directions and $U = [\rho \ \rho Y_g \ \rho u_1 \ \rho u_2 \ \rho u_3]^T$ is the conservative solution vector, ρ is the mixture density, ρY_g is the gas mass fraction and ρu is the mixture momentum. Here the absence of the energy equation is due to the barotropic approach, whereas a transport equation for modelling the non-condensable gas phase is used. The flux tensor F consists of the convective and viscous terms and can be analysed into x , y and z components: $F = [F_1 \ F_2 \ F_3]$,

where:

$$F_1 = \begin{bmatrix} \rho u_1 \\ \rho Y_g u_1 \\ \rho u_1^2 + p - \tau_{11} \\ \rho u_1 u_2 - \tau_{12} \\ \rho u_1 u_3 - \tau_{13} \end{bmatrix}, \quad F_2 = \begin{bmatrix} \rho u_2 \\ \rho Y_g u_2 \\ \rho u_2 u_1 - \tau_{21} \\ \rho u_2^2 + p - \tau_{22} \\ \rho u_2 u_3 - \tau_{23} \end{bmatrix}, \quad F_3 = \begin{bmatrix} \rho u_3 \\ \rho Y_g u_3 \\ \rho u_3 u_1 - \tau_{31} \\ \rho u_3 u_2 - \tau_{32} \\ \rho u_3^2 + p - \tau_{33} \end{bmatrix} \quad (2)$$

For Newtonian fluids the viscous stress tensor is given by the relation:

$$\tau_{ij} = \mu \left(\frac{\partial u_i}{\partial x_j} + \frac{\partial u_j}{\partial x_i} - \frac{2}{3} \frac{\partial u_k}{\partial x_k} \delta_{ij} \right), \quad i, j, k = 1, 2, 3. \quad (3)$$

A homogeneous-mixture approach is used for describing the liquid, liquid-vapour regime (referred as mixture from now on) and gas phases, which means that the three phases are in mechanical and thermal equilibrium. Then the single fluid model for the liquid and mixture is extended by a transport equation for the non-condensable gas. The thermodynamic closure is achieved by a linear barotropic model for the liquid and the mixture in addition to an isothermal ideal gas model, which has been employed for the gas [55]. In order to calculate the pressure of the mixture, a quadratic equation has been solved. The mixture density ρ is:

$$\rho = \beta_{lm} [(1 - \alpha_v) \rho_l + \alpha_v \rho_v] + \beta_g \rho_g, \quad (4)$$

In the above relations, the subscripts l, m, g represent the liquid, mixture and gas regimes respectively. The linear barotropic model for the liquid and the mixture is:

$$\rho_{lm} = \rho_{l,sat} + \frac{1}{c^2} (p - p_{sat}), \quad c = \begin{cases} c_l, & p \geq p_{sat} \\ c_m, & p < p_{sat} \end{cases} \quad (5)$$

where $\rho_{l,sat}$ is the density of the liquid at saturation condition and c is the speed of sound of the liquid or the mixture, depending on the saturation pressure p_{sat} . Phase-change between liquid and vapour is modelled by the density variation (HEM assumption) [55, 54]; if the density found from the continuity equation is below the saturation density $\rho_{l,sat} = 998.17 \text{ kg/m}^3$, vapour is generated. The gas phase has been modelled by an isothermal ideal gas EoS and thus, the gas density is given by:

$$\rho_g = \frac{p}{R_g T_{ref}}, \quad (6)$$

By differentiating pressure with respect to density, the speed of sound is constant for each phase and can vary from 1 m/s in the mixture regime, up to 1482.35 m/s in the liquid region, whereas in the gaseous phase the speed of sound is 290 m/s [55]. The density of the component $i = l, m, g$ can be found from:

$$\rho_i = \frac{m_i}{V_i} = \frac{Y_i m}{\beta_i V} = \frac{Y_i}{\beta_i} \rho, \quad (7)$$

where β is the volume fraction of the i component:

$$\beta_i = \frac{V_i}{V}, \quad \sum_i \beta_i = 1, \quad (8)$$

Y_i is the mass fraction of the i component:

$$Y_i = \frac{m_i}{m}, \quad \sum_i Y_i = 1, \quad (9)$$

and the local volume fraction can be calculated from the formula:

$$\alpha_v = \begin{cases} 0, & \rho \geq \rho_{l,sat} \\ \beta_{lm} \frac{\rho_{l,sat} - \rho_{lm}}{\rho_{l,sat} - \rho_{v,sat}}, & \rho < \rho_{l,sat} \end{cases} \quad (10)$$

Due to the large variation in the speed of sound, the Mach number in three phase flows can range from 10^{-2} up to 10^2 or even higher [56]. In order to handle the low Mach number problem, a hybrid flux, suitable for multiphase flows, is utilised [54].

The aforementioned flux is based on the Primitive Variable Riemann Solver (PVRS) [57] and the Mach consistent numerical flux of Schmidt et al. [58]. At the same time, the numerical scheme is suitable for subsonic up to supersonic flow conditions. The numerical flux in the k direction at the $i+1/2$ interface takes the following form:

$$F_k^{i+1/2} = \rho^{L/R} u_k^{\hat{a}} \begin{bmatrix} 1 \\ Y_g^{L/R} \\ u_1^{L/R} \\ u_2^{L/R} \\ u_3^{L/R} \end{bmatrix} + p^{\hat{a}} \begin{bmatrix} 0 \\ 0 \\ \delta_{1k} \\ \delta_{2k} \\ \delta_{3k} \end{bmatrix}, \quad (11)$$

where the interface velocity $u_k^{\hat{a}}$ is approximated by:

$$u_k^{\hat{a}} = \frac{1}{C^L + C^R} [C^L u_k^L + C^R u_k^R + (p^L - p^R)], \quad (12)$$

and C is the acoustic impedance $C = \rho c$. The interface pressure $p^{\hat{a}}$ is:

$$p^{\hat{a}} = (1-b)p^{\hat{a},incr} + bp^{\hat{a},comp}. \quad (13)$$

In Eq. (13), the interface pressure is the sum of the incompressible and the compressible parts, where the incompressible contribution is:

$$p^{\hat{a},incr} = \frac{C^L p^R + C^R p^L}{C^L + C^R}, \quad (14)$$

and the compressible contribution is:

$$p^{\hat{a},comp} = \frac{C^L p^R + C^R p^L + C^R C^L (u_k^L - u_k^R)}{C^L + C^R} \quad (15)$$

Depending on the Mach number, the contribution of the incompressible or the compressible part in Eq. (13) is more dominant and the weighted term b is :

$$b = 1 - e^{-dM}, \quad (16)$$

where the Mach number M is defined as:

$$M = \max\left(\frac{|u^L|}{c^L}, \frac{|u^R|}{c^R}\right). \quad (17)$$

The blending coefficient is $d : (10,100)$. For incompressible single phase flow, Eq. (14) is taking the form of $\frac{1}{2}(p_L + p_R)$ since $c^L = c^R$. However, for two-phase flows, Eq. (14) is much closer to the exact solution.

A four stage Runge-Kutta (RK), 4th order accurate in time has been implemented for time advancement [57], in order to capture the waves which are propagating in the domain.

3 Results

In this section, numerical simulations of the needle-free device are presented for several different initial conditions, regarding the pressure of the gas bubble and the geometry of the interface between the water and the air. First, results for the conventional meniscus design and comparison with experimental values are shown. Then, a parametric study for different values of the bubble pressure is performed as another mean of validating the methodology. In the end, different meniscus geometries have been simulated in order to find a design appropriate for needle-free devices, ensuring focused high speed jets. The different cases examined are summarised in Table 0.

Table 1: Numbering, meniscus geometry, pressure of the gas bubble, Reynolds and Weber numbers. The Reynolds and Weber numbers are calculated based on the jet diameter and the maximum jet velocity. The dynamic viscosity of water is $\mu_l = 0.001 Pa \cdot s$ and the water surface tension is $\sigma = 0.072 N / m$. Trumpet shape is referred to a meniscus geometry combining the features of the hemispherical and the conical shapes (see Fig. 3.3).

Name	Meniscus geometry	P_{bub} (Pa)	Re	We
case 1	hemispherical	$2 \cdot 10^7$	388	84.3
case 2	hemispherical	$3.7 \cdot 10^7$	459	118
case 3	hemispherical	$5 \cdot 10^7$	704	278
case 4	hemispherical	$7 \cdot 10^7$	839	394
case 5		$1 \cdot 10^8$	1105	683

	hemispherical			
case 6	hemispherical	$1.35 \cdot 10^8$	1245	866
case 7	hemispherical	$1.5 \cdot 10^8$	1411	1110
case 8	conical	$5 \cdot 10^7$	120	80
case 9	trumpet	$5 \cdot 10^7$	423	1000

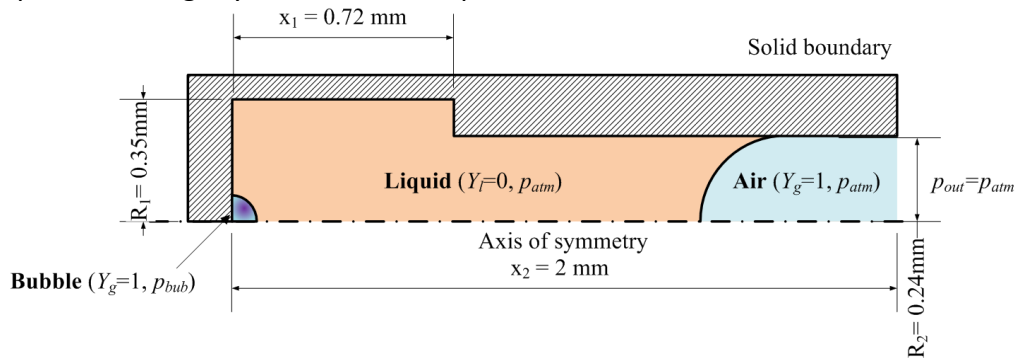
3.1 Numerical simulation

The geometry of the device is taken from [9] and can be seen in Fig. 3.3. Since the problem is axisymmetric, a structured-mesh wedge of 5° angle is employed with approximately $90k$ equally spaced cells with $\Delta x = 2.5 \cdot 10^{-6} m$ (Fig. 3.1). The upper and the left sides of the wedge have been set as no-slip wall, whereas in the right side, the pressure is specified (atmospheric). Initially, compressed gas (different initial pressure p_{bub} depending on the case examined) is in the hemispherical bubble (gas mass fraction $Y=1$), which is in the centre of the left wall, while the water ($Y=0$) and the air ($Y=1$) are in atmospheric conditions (p_{atm}), as it is shown in Fig. 3.1. The liquid phase is left to the meniscus and the gas phase is on the right side of the meniscus. The initial density in each phase is determined from the barotropic EoS.

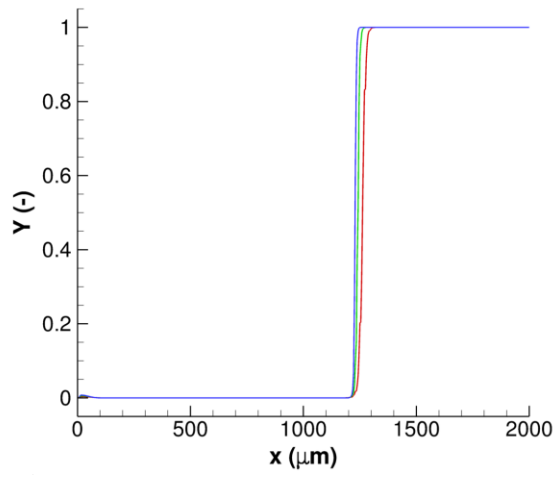
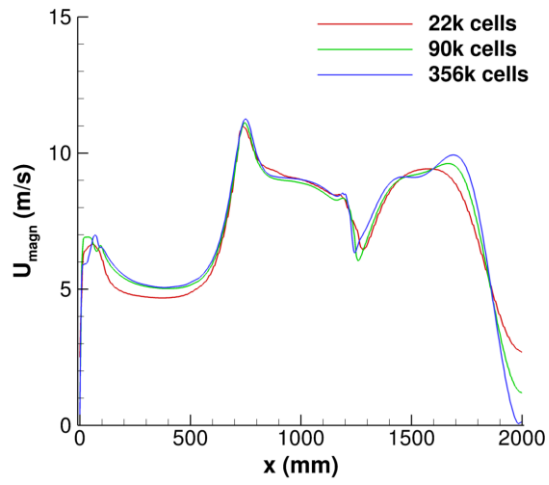
For the grid independence study, three different meshes have been employed for case 3, $22k$ cells (coarse grid), $90k$ cells (intermediate grid) and $356k$ cells (fine grid). In Fig. 3.1 the velocity magnitude (left) and the gas mass fraction (right) values along the x-axis are plotted ($y=175 \mu m$) at $t=10 \mu s$. While in general the three grids are in good agreement, there are small deviations in the velocity plot. The deviation close to the origin of x axis is due to the more accurate representation of the bubble in higher resolution grids. Concerning the velocity of the jet ($x > 1mm$) and how its magnitude depends on the grid resolution, more diffusive solution is obtained with a coarse grid and therefore smaller velocity fluctuations are noticed in velocity plot of Fig. 3.1. The intermediate grid has been selected, since it is in satisfactory agreement with the dense one.

In Fig. 3.1 the pressure ($x-y$ plane) and velocity magnitude ($x-z$ plane) contours are shown, combined with iso-surfaces for the vapour (white) and the air (pink) phases. At time instant $t=1.5 \mu s$ the pressure wave has already been reflected at the meniscus resulting in the initialisation of an axisymmetric microjet. Apart from the aforementioned mechanism, the focusing in the nozzle is also responsible for the acceleration of the flow [40, 17] (see also Fig. 3.2). In the next frame ($t=13.5 \mu s$), the jet and a cavitation regime along the wall have been formed. At time instant $t=20 \mu s$ the cavitation area has been formed and the the jet has moved forward.

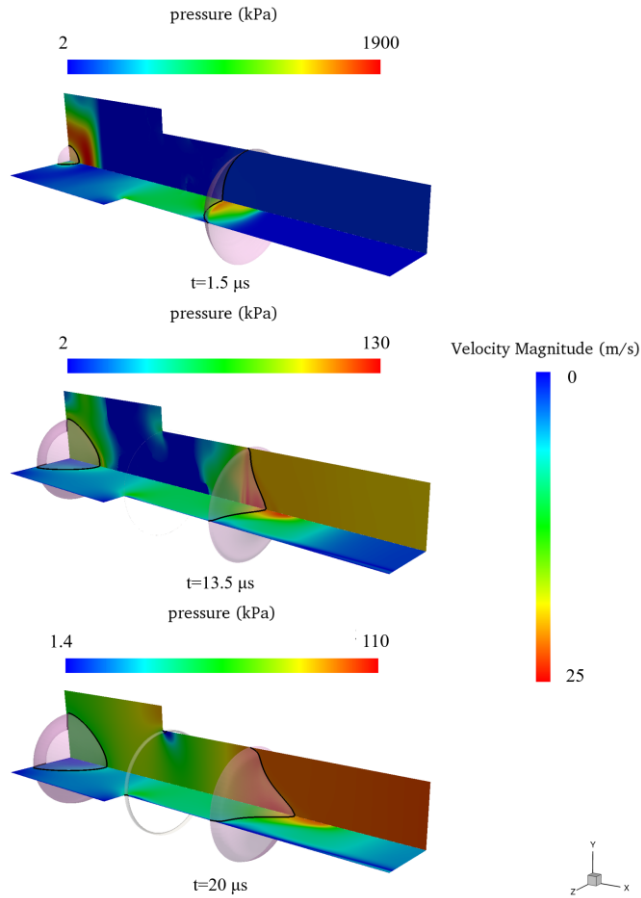
Comparison with experimental results of Hayasaka et al. [9] is shown in Fig. 3.1. The correspondence between the laser energy in the experiment and the pressure of the hemispherical bubble which has been used as initial condition in the simulation, is achieved by equalising the laser energy with the dynamic energy of the bubble. The dynamic energy of the bubble is calculated from $E_{dyn} = \Delta p V$, where $\Delta p = p_{bub} - p_l$ with p_{bub} and p_l being the pressure of the bubble and the liquid respectively and V is the volume of the hemisphere. Because of the barotropic EoS, the heat absorbed from the bubble is not taken into account and thus, a calibrating coefficient n is used in order for the dynamic energy of the bubble to match the absorbed laser energy: $E = n\Delta p V$ (in the present study $n=151$). Overall, the experimental and the numerical values are in satisfactory agreement, as the same pattern is noticed: initially high jet velocities were measured and then an asymptotic decrease of the jet velocity follows. However, in the last points which correspond to the largest available distances, the decrease rate of the jet velocity with respect to distance is slightly smaller in the simulations, compared to the experimental data. This discrepancy in the results is due to the visual approximation of the initial meniscus shape in the simulations, which is roughly replicated from the experiment based on a figure. The jet evolution is strongly affected by the meniscus shape, as it will be shown in section 3.3 and hence, even small differences between the approximated shape and the one created in the experiments can cause deviation in the jet velocity. Another reason is the inconsistency between the 0° and 90° experimental data [9], which is more evident for the higher energy experiments. The 0° data have a more abrupt decrease of the jet velocity and significantly larger error bars. The simulation points are either in the range of the 0° experimental points or in the 90° points, while for larger distances the simulation points are slightly above the 90° points.



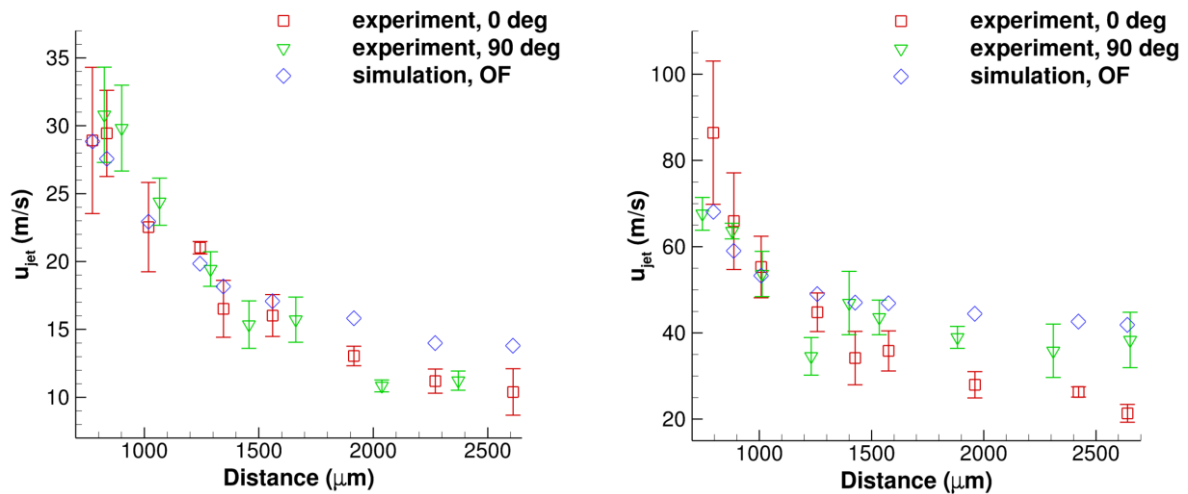
Needleless injection configuration for the hemispherical meniscus geometry: the computational domain (liquid, air, bubble), liquid-gas interface (black line), solid boundary (dashed area) and axis of symmetry (dash dot line).



Grid independence study for the needle-free device. Plots of velocity magnitude (left) and gas mass fraction(right) along a line parallel to the x-axis ($y = 175 \mu\text{m}$) at $t = 10 \mu\text{s}$.



2-D axisymmetric needle-free device simulation for $p_{bub} = 5 \cdot 10^7 Pa$ and the standard meniscus shape (*case 3*). Pressure field on the $x-y$ plane and velocity magnitude field on the $x-z$ plane are shown, combined with iso-surfaces for vapour volume fraction $\alpha = 0.5$ (white) and iso-surface for gas volume fraction $B_g = 0.5$ (pink).



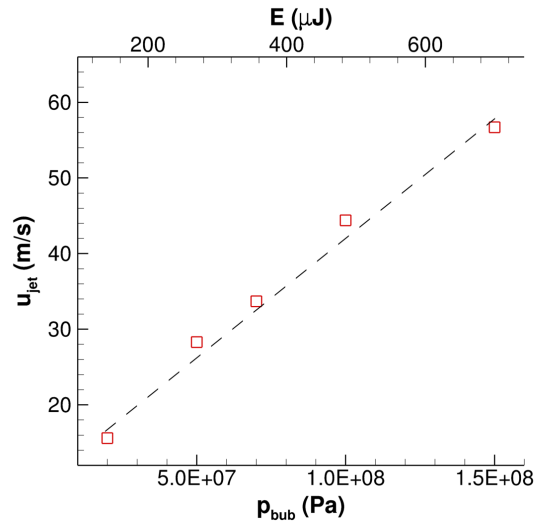
Comparison of *case 2* and *case 6* with experimental data of Hayasaka et al. [9]. Jet velocity as a

function of the distance between the bubble and the air-liquid interface ($B_g = 0.5$) for laser energy $185\mu J$ (left) and $650\mu J$ (right).

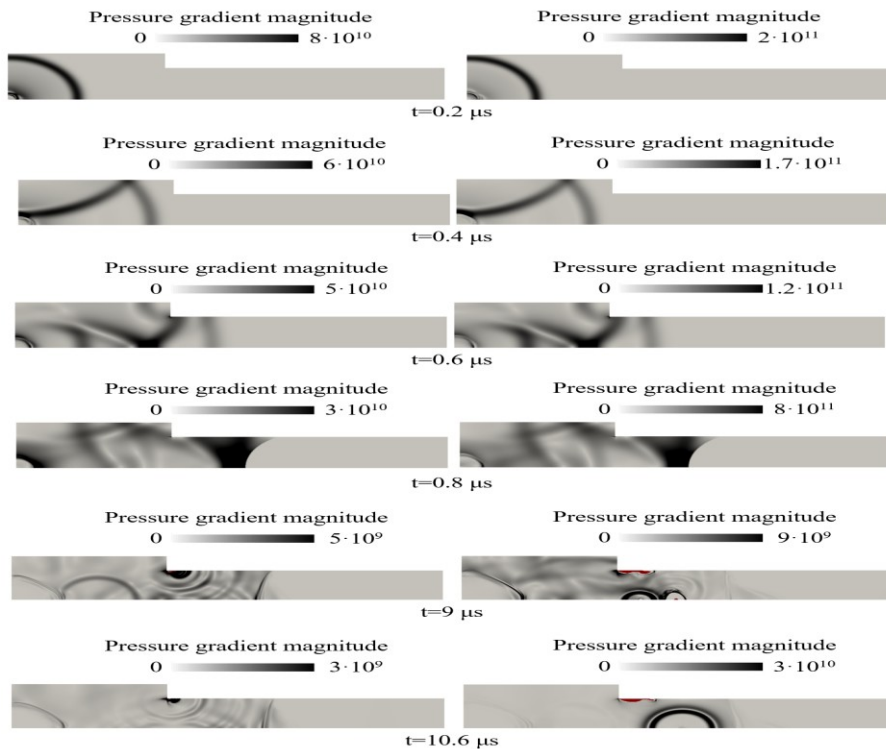
3.2 Dependence on the bubble pressure

Several simulations have been performed for different values of the bubble pressure (*case 1-case 7*). In Fig. 3.2 the linear relation between the bubble pressure or the absorbed laser energy and the jet velocity is shown. The laser energy is calculated from the dynamic pressure of the bubble, as explained in 3.1. Similar findings have been reported in the experimental work of Tagawa et al. [18] and in the numerical work of Peters et al. [17]. In the latter, they modelled the pressure wave by a pressure pulse on the bubble and they demonstrated the linear correlation between the pressure pulse and the jet velocity. The fact that the linear function is not intercepted at $u_{jet} = 0$, means that a jet is formed even for lower values of absorbed laser energy and there is no threshold heat, in contrary to the previous studies of Tagawa et al. [18] and of Peters et al. [17]. This is due to the energy that has been spent in the experiment in order to heat the fluid before vaporisation [30]. In the simulations of Peters et al. [17], surface tension is responsible for the threshold, whereas in the present work surface tension is not modelled and therefore there is not such a threshold.

In Fig. 3.2 the magnitude of the pressure gradient is shown for *case 3* and *case 7* combined with vapour volume fraction iso-lines of $\alpha = 0.5$ (red). For the first four time instances plotted, the pattern is similar for both cases since the wave emanating from the bubble travels at almost the same wave speed ($u + c$). In the first time instance plotted ($t = 0.2\mu s$), the shock wave, which has been emitted by the bubble, travels in the liquid. At $t = 0.4\mu s$ it has already been reflected from the upper horizontal wall and the reflection of the wave has reached the bubble, while the original wave moves to the positive direction of the x axis. At $t = 0.6\mu s$ the superposition of three waves travel in the liquid. The original wave is advancing into the capillary, while its previous reflection has been reflected again from the upper vertical wall and it is moving towards the negative direction of the x axis. Apart from those two waves, another reflection at the bubble moves upwards. At $t = 0.8\mu s$ the original wave is reflected at the meniscus and the formation of the jet starts. Due to higher bubble pressure in *case 7*, the jet has travelled a longer distance in the capillary compared to *case 3*, as it can be seen at $t = 9\mu s$. In addition, cavitation regions have been formed in the upper wall for both cases; however in *case 7* the vapour phase is much more extended and there is an additional vapour regime close to the axis of symmetry, because of the stronger shock wave. Although a similar low pressure exists in *case 3*, vapour is not generated, as the pressure is slightly above the saturation pressure. In the last time instant plotted ($t = 10.6\mu s$), a new shock wave is noticed in *case 7*, emanating from the collapse of the vaporous bubble, something which is not observed in *case 3*.



The influence of the bubble pressure on the jet velocity.



Slice on the $x-y$ plane for $z=0$. Magnitude of the pressure gradient; regimes of vapour volume fraction $\alpha \geq 0.5$ are coloured in red for *case 3* (left) and *case 7* (right).

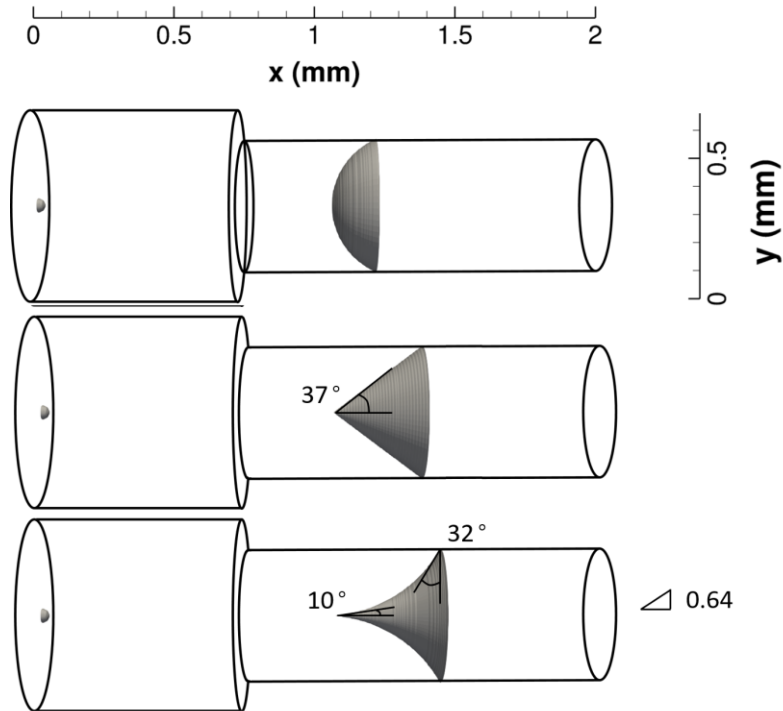
3.3 Dependence on the free surface geometry

In this section the sensitivity of the meniscus geometry to the jet velocity is investigated. Based on shaped charge jets, three different geometries for the free surface have been utilised as initial condition: the hemispherical free surface shape (*case 3*), the conical shape (*case 8*) and

the trumpet shape (*case 9*), as they are shown in Fig. 3.3. The hemispherical shape has been also adopted in previous experimental works by dipping the tip of the tube in a hydrophobic solution [18]. In practice, as it has been denoted in previous works [59, 60], it may not be easy to achieve the conical and the trumpet shapes of the meniscus. In Table 1 the maximum jet velocity and the jet diameter are summarised. It is evident that by utilising the trumpet shape for the meniscus geometry, jet velocity has the maximum value among the three cases, while at the same time the diameter of the jet remains small. The jet diameter of *case 3* is one order of magnitude smaller than the diameter of the capillary, while the jet diameters of *case 8* and *case 9* are one order of magnitude smaller than *case 3*.

The contact angle between the free surface geometry and the wall determines the focusing of the flow. In the worst case scenario, if the contact angle is 90 degrees, a flat free surface is created, the liquid moves in the tube parallel to the walls and no jet is formed. On the other hand, a contact angle of 0 degrees results in curvature equal to the radius of the capillary. As the contact angle becomes smaller, the focusing is increased, resulting in higher jet velocities [18, 39, 17]. In Fig. 3 the vectors on the liquid-gas interface of the capillary are shown, combined with red iso-line of gas volume fraction $B_g = 0.5$ for *case 3*, *case 8* and *case 9*. From the vector field at three time frames the increased focusing in the conical and trumpet meniscus is evident, since more liquid volume is on the tip of the interface. On the other hand, in the hemispherical shape the vectors are almost parallel which means reduced focusing. It can be also concluded that the evolution of the jet is much faster in *case 8* and *case 9* and that the jet diameter in *case 3* is much larger compared to the other two cases ($t = 10 \mu s$). In shaped charges, similar shape for the liner is used with similar effects on the hole diameter and the penetration depth. As it has been explained in 1, conical liner results in deeper penetration and a small hole diameter, whereas hemispherical liner create a larger diameter and shallow penetration [24, 22, 21, 23].

In Fig. 4 and 5 the pressure ($x-y$ plane) and the velocity magnitude ($x-z$ plane) contours are shown combined with iso-surfaces for the vapour (white) and the air (pink) phases. Similar to Fig. 3.1, the first time frame is just after the reflection of the wave at the meniscus interface and the initialisation of the jet is shown. In the second and the third frames, the jet has been formed and advances in the capillary, while cavitation areas have been identified. The jets with the conical and trumpet initialisation are more focused and have larger velocity magnitude than the hemispherical shape (see also Table 1 and Fig. 3).



Initial condition of the meniscus, from top to bottom: hemispherical initialisation (*case 3*), conic initialisation (*case 8*) and trumpet initialisation (*case 9*). The opening angle of the cone in *case 8* is 37° . The trumpet aspect ratio in *case 9* is 0.64 , the contact angle between the interface and the y axis is 32° and the opening angle of the discretized interface is 10° .

Table 2: The effect of the meniscus geometry on the maximum jet velocity and on the jet diameter for $p_{bub} = 5 \cdot 10^7 Pa$.

Meniscus geometry	u_{jet} (m/s)	D_{jet} (μm)
hemispherical	28.3	25
conical	48	2.5
trumpet	170	2.5

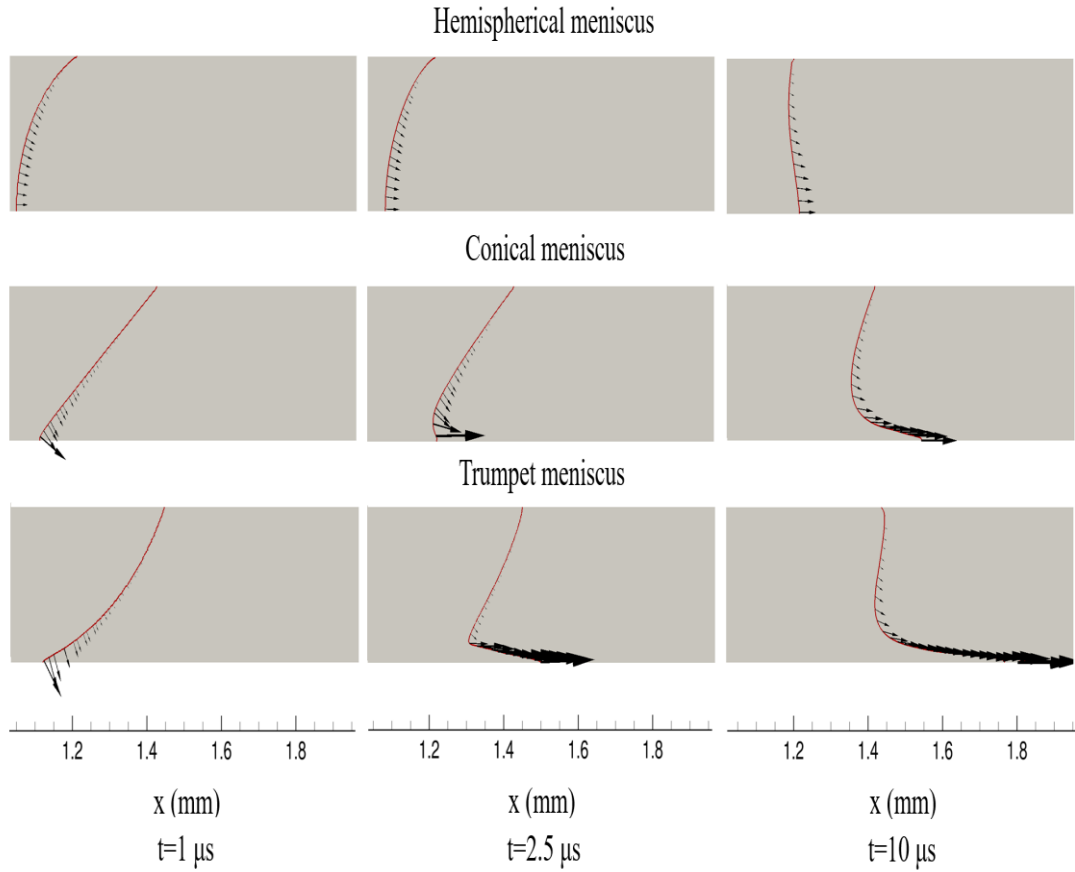


Table 3: Slice on the $x-y$ plane for $z=0$. Vector field on the interface, for gas volume fraction $B_g = 0.5$ (red iso-line). From top to bottom: hemispherical initialisation (*case 3*), conic initialisation (*case 8*) and trumpet initialisation (*case 9*). The magnitude of the vectors is proportional to the velocity magnitude.

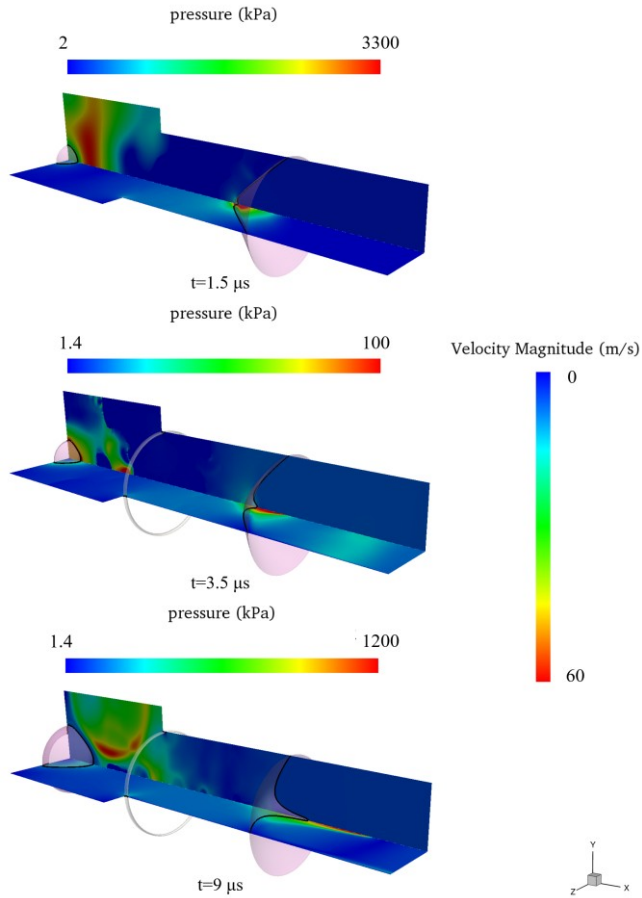


Table 4: 2-D axisymmetric needle-free device simulation for $p_{bub} = 5 \cdot 10^7 Pa$ and the conical meniscus shape (case 8). Pressure field on the $x-y$ plane and velocity magnitude field on the $x-z$ plane are shown, combined with iso-surface for vapour volume fraction $\alpha = 0.5$ (white) and iso-surface for gas volume fraction $B_g = 0.5$ (pink).

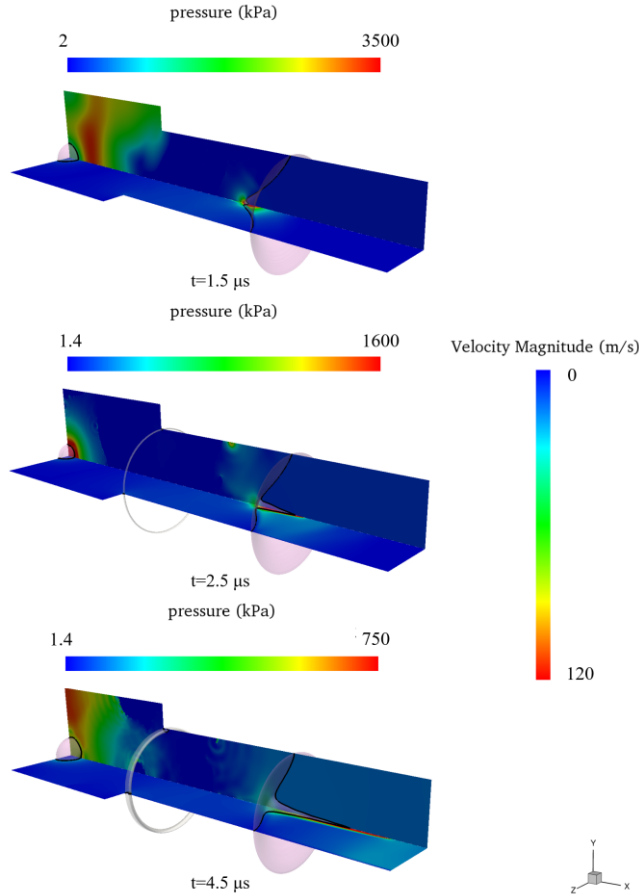


Table 5: 2-D axisymmetric needle-free device simulation for $p_{bub} = 5 \cdot 10^7 Pa$ and the trumpet meniscus shape (case 9). Pressure field on the $x-y$ plane and velocity magnitude field on the $x-z$ plane are shown, combined with iso-surface for vapour volume fraction $\alpha = 0.5$ (white) and iso-surface for gas volume fraction $B_g = 0.5$ (pink).

4 Conclusions

In the present work, a simulation of a needle-free device has been performed by utilising an explicit density-based solver able to model the co-existence of gaseous, liquid and vapour phases. The validity of the results has been assessed by comparison with experimental values and by demonstrating a linear relation between the laser energy and the jet velocity. Then, the influence of the meniscus shape on the jet velocity has been studied, by simulating cases with a hemispherical, a conical and a trumpet shape interface between the liquid and the atmospheric air. The trumpet shape, which initially resembles to a cone and then takes a spherical shape, was found to give focused microjets, while the velocity magnitude of the jet was the maximum among the cases examined. The critical jet velocity (u_{cr}) for skin penetration is approximated by equalizing the water hammer pressure (p_{wh}) with the yield stress of the human skin, which has an average value of $15MPa$ [61]. In the cases simulated the jet velocity

is by far larger than the $u_{cr} = 10m/s$ and therefore, the formed jet is strong enough to penetrate the skin. In addition, the jet diameter when using the conical or the trumpet shape in the interface, was found to be one order of magnitude smaller than the jet diameter noticed with the hemispherical meniscus shape. Assuming there is a good reproducibility of such experiments and the trumpet or the conical interface between the medicine and the air can be formed, such studies can offer insight towards a new needle-free design.

Appendix

5 Riemann problem (Validation)

The Riemann problem is an Initial Value Problem (IVP) with a discontinuity at x_0 [57]:

$$\mathbf{U}(x, t = 0) = \begin{cases} \mathbf{U}_L(x), & x < x_0 \\ \mathbf{U}_R(x), & x \geq x_0 \end{cases} \quad (18)$$

For the purpose of validation, the 1-D Euler Riemann problem is considered next, with two different constant states on the left (\mathbf{U}_L) and right (\mathbf{U}_R). Validation of the PVRs-solver is provided in this section, by comparing the exact $p^{\hat{a}}$ and $u^{\hat{a}}$ values with the numerical ones for three different demanding Riemann problems. Only a small deviation from the exact solutions is noticed.

5.0.1 Case A

The initial configuration of the Riemann problem is shown in Table 5. The exact solution is $p^{\hat{a}} = 1430.9Pa$ and $u^{\hat{a}} = 0.067m/s$. The PVRs-solver outlined in section 2, predicts $p^{\hat{a}} = 1430.9Pa$ (practically identical to exact solution) and $u^{\hat{a}} = 0.066m/s$ (0.2 % deviation from exact).

Table 6: Initial configuration for the Riemann problem of 5.0.1.

<i>material-1,</i> $x < 0$ (Liquid)	<i>material-2,</i> $x \geq 0$ (Gas)
$\rho_L = 998$	$\rho_R = 0.017kg / m^3$
$u_L = 0m/s$	$u_R = 0m/s$
$p_L = 999$	$p_R = 1400Pa$

5.0.2 Case B

The second Riemann problem is a much more demanding case, since there is a huge pressure and density variation between the L, R states. The initial configuration of this Riemann problem is shown in Table 6. The exact solution is $p^{\hat{a}} = 144.4 Pa$ and $u^{\hat{a}} = 2.73 m/s$. The PVRS-solver outlined in section 2, predicts $p^{\hat{a}} = 144.4 Pa$ (practically identical to exact solution) and $u^{\hat{a}} = 2.72 m/s$ (0.32 % deviation from exact).

Table 7: Initial configuration for the Riemann problem of 5.0.2.

<i>material-1,</i> $x < 0$ (Liquid)	<i>material-2,</i> $x \geq 0$ (Gas)
$\rho_L = 100$	$\rho_R = 0.0017 kg / m^3$
$u_L = 0 m / s$	$u_R = 0 m / s$
$p_L = 40.4 Pa$	$p_R = 143 Pa$

5.0.3 Case C

In this case, although the pressure and density ratios are much lower than the case in section 5.0.2, the challenge is to predict the induced depressurization due to the high gas velocity. The initial configuration of this Riemann problem is shown in Table 7. The exact solution is $p^{\hat{a}} = 81548 Pa$ and $u^{\hat{a}} = 2.68 m/s$. The PVRS-solver outlined in section 2, predicts $p^{\hat{a}} = 82025 Pa$ (0.59 % deviation from exact solution) and $u^{\hat{a}} = 2.67 m/s$ (0.33 % deviation from exact).

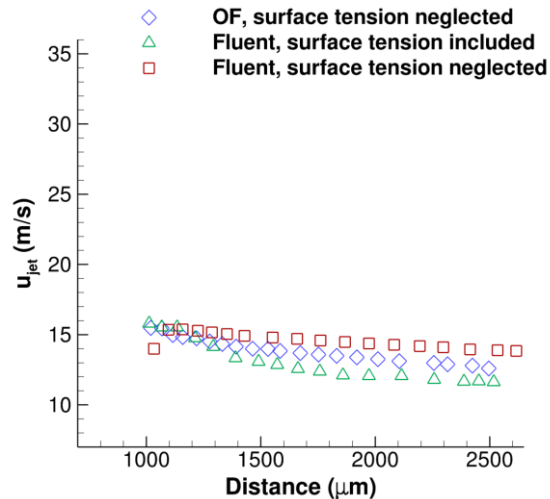
Table 8: Initial configuration for the Riemann problem of 5.0.3.

<i>material-1,</i> $x < 0$ (Liquid)	<i>material-2,</i> $x \geq 0$ (Gas)
$\rho_L = 100$	$\rho_R = 1 kg / m^3$
$u_L = 0 m / s$	$u_R = 10 m / s$
$p_L = 40.4 Pa$	

$p_R = 84151Pa$

6 The effect of surface tension

Given the high We number, surface tension effects are not dominant in the current study. In order to demonstrate that, simulations with and without surface tension have been performed for *case 1*, which has one of the lowest We numbers ($We=84.3$). The present solution in OF is compared against solutions obtained in Ansys Fluent CFD package with and without surface tension. The numerical model in Fluent is similar to the one that has been developed in OF: a barotropic EoS has been utilised for modelling the phase-change between the liquid and the vapour, accompanied by a VOF scheme for the gas phase, either considering or neglecting surface tension. In Fig. 6 the jet velocity with respect to the time-varying distance between the bubble and the gas-liquid interface for $p_{bub} = 2 \cdot 10^7$ is plotted for the 3 different models. It has to be clarified here that the distance in the below figure is different than the distances measured in Fig. 3.1, as here all points correspond to a single case and the distance is a function of time. As it can be seen in Fig. 6, the differences when considering surface tension or not are insignificant and thus, such effects can be ignored.



The effect of surface tension is assessed by plotting the jet velocity as a function of the distance between the bubble and the gas-liquid interface for *case 2*. Comparison between the present work in OF, where surface tension was neglected (blue diamond) and Fluent simulations where surface tension was either considered (green triangle) or neglected (red square).

The data are available in the following link:
<https://gitlab.com/NikolausK/needleFreeSims.git>

N.K. implemented the algorithm in OF, created the meshes, performed the simulations, post-processed the results and wrote the paper. P.K. performed the numerics development. M.G. provided the funding and supervised the research. All authors reviewed the paper and

gave final approval for publication.

The authors have no competing interests.

The research leading to these results has received funding from the MSCA-ITN-ETN of the European Union's H2020 programme, under REA grant agreement n. 642536.

The authors would also like to acknowledge the contribution of The Lloyd's Register Foundation. Lloyd's Register Foundation helps to protect life and property by supporting engineering-related education, public engagement and the application of research.

References

- [1] Mitragotri S. 2006 Current status and future prospects of needle-free liquid jet injectors. *Nature Reviews Drug Discovery* **5**, 543–.
- [2] Berrospe-Rodriguez C, Visser CW, Schlautmann S, Ramos-Garcia R, Rivas DF. 2016 Continuous-wave laser generated jets for needle free applications. *Biomicrofluidics* **10**, 014104.
- [3] Ravi AD, Sadhna D, Nagpaal D, Chawla L. 2015 Needle free injection technology: A complete insight. *International Journal of Pharmaceutical Investigation* **5**, 192–199.
- [4] Kendall M. 2006 Engineering of needle-free physical methods to target epidermal cells for DNA vaccination. *Vaccine* **24**, 4651 – 4656. DNA Vaccines.
- [5] Arora A, Prausnitz MR, Mitragotri S. 2008 Micro-scale devices for transdermal drug delivery. *International Journal of Pharmaceutics* **364**, 227 – 236. Future Perspectives in Pharmaceutics Contributions from Younger Scientists.
- [6] Kale TR, Momin M. 2014 Needle free injection technology - An overview. *INNOVATIONS in pharmacy* **5**, 1–8.
- [7] Giudice EL, Campbell JD. 2006 Needle-free vaccine delivery. *Advanced Drug Delivery Reviews* **58**, 68 – 89. Challenges in Pediatric Drug Delivery: the Case of Vaccines.
- [8] Zogenix. 2009 SUMAVELTM DoseProTM (sumatriptan injection) Needle-Free

Delivery System. <http://www.zogenix.com/docs/pk/Sumavel-DosePro-Fact-Sheet.pdf>.

[9] Hayasaka K, Kiyama A, Tagawa Y. 2017 Effects of pressure impulse and peak pressure of a shockwave on microjet velocity in a microchannel. *Microfluidics and Nanofluidics* **21**, 166.

[10] Han T, Hah J, Kim S, Yoh JJ. 2012 pp. 819–825. In *Light syringes based on the laser induced shock wave*, vol. 2, *28th International Symposium on Shock Waves* pp. 819–825. Springer.

[11] Park MA, Jang HJ, Sirotkin FV, Yoh JJ. 2012 Er:YAG laser pulse for small-dose splashback-free microjet transdermal drug delivery. *Opt. Lett.* **37**, 3894–3896.

[12] Yoh JJ, Jang HJ, Park Ma, Han Th, Hah Jm. 2012 A laser syringe aimed at delivering drug into the outer layer of human skin. *AIP Conference Proceedings* **1464**, 524–531.

[13] Han Th, Yoh JJ. 2010 A laser based reusable microjet injector for transdermal drug delivery. *Journal of Applied Physics* **107**, 103110.

[14] Loske AM. 2017 *Medical and Biomedical Applications of Shock Waves*. Shock Wave and High Pressure Phenomena. Springer International Publishing.

[15] Canter J, Mackey K, Good LS, et al. 1990 An outbreak of hepatitis b associated with jet injections in a weight reduction clinic. *Archives of Internal Medicine* **150**, 1923–1927.

[16] Antkowiak A, Bremond N, Le Dizès S, Villermaux E. 2007 Short-term dynamics of a density interface following an impact. *Journal of Fluid Mechanics* **577**, 241–250.

[17] Peters IR, Tagawa Y, Oudalov N, Sun C, Prosperetti A, Lohse D, van der Meer D. 2013 Highly focused supersonic microjets: numerical simulations. *Journal of Fluid Mechanics* **719**, 587–605.

[18] Tagawa Y, Oudalov N, Visser CW, Peters IR, van der Meer D, Sun C, Prosperetti A, Lohse D. 2012 Highly Focused Supersonic Microjets. *Phys. Rev. X* **2**, 031002.

[19] Held M. 1989 Fundamentals of shaped charges. William P. Walters and Jonas A. Zukas. John Wiley & Sons, New York 1989, 398 pp., ISBN 0-471-62172-2. *Propellants, Explosives, Pyrotechnics* **14**, 220–220.

[20] Katz JI. 1999 Jets from collapsing bubbles. *Proceedings of the Royal Society of London A: Mathematical, Physical and Engineering Sciences* **455**, 323–328.

[21] Arvidsson B, Ohlsson HG. 1984 Investigation of Liners For Shaped Charges Manufactured from Cu-Powder by X-ray Diffraction and Ultrasonic Techniques. Orlando, Florida. 8th International Symposium on Ballistics.

[22] Chou PC, Ciccarelli RD, Walters WP. 1983 The formation of Jets from Hemispherical-Linear Warheads. The Hague, Netherlands. 7th Int. Symp. on Ballistics.

[23] Davison DK, Arvidsson BK. 1985 Optimization of a 90 mm Shaped Charge Warhead. Panama City Beach, Florida. 2nd Symposium on the Interaction of Non-Nuclear Munitions with Structures.

[24] Lee WH. 2006 *Computer Simulation of Shaped Charge Problems*. World Scientific.

[25] Benjamin TB, Ellis AT. 1966 The Collapse of Cavitation Bubbles and the Pressures thereby Produced against Solid Boundaries. *Philosophical Transactions of the Royal Society of London. Series A, Mathematical and Physical Sciences* **260**, 221–240.

[26] Field JE. 1966 A discussion on deformation of solids by the impact of liquids, and its relation to rain damage in aircraft and missiles, to blade erosion in steam turbines, and to cavitation erosion - Stress waves, deformation and fracture caused by liquid impact. *Philosophical Transactions of the Royal Society of London A: Mathematical, Physical and Engineering Sciences* **260**, 86–93.

[27] Plesset MS, Chapman RB. 1971 Collapse of an initially spherical vapour cavity in the neighbourhood of a solid boundary. *Journal of Fluid Mechanics* **47**, 283–290.

[28] Longuet-Higgins MS. 1983 Bubbles, breaking waves and hyperbolic jets at a free

surface. *Journal of Fluid Mechanics* **127**, 103–121.

[29] Longuet-Higgins MS, Oguz H. 1995 Critical microjets in collapsing cavities. *Journal of Fluid Mechanics* **290**, 183–201.

[30] Sun C, Can E, Dijkink R, Lohse D, Prosperetti A. 2009 Growth and collapse of a vapour bubble in a microtube: the role of thermal effects. *Journal of Fluid Mechanics* **632**, 5–16.

[31] Leighton T, Ho W, Flaxman R. 1997 Sonoluminescence from the unstable collapse of a conical bubble. *Ultrasonics* **35**, 399–405.

[32] Leighton TG, Phelps AD, Cox BT, Ho WL. 1998 Theory and preliminary measurements of the Rayleigh-like collapse of a conical bubble. *Acta Acustica united with Acustica* **84**, 1014–1024 (11).

[33] Leighton T, Cox B, Birkin P, Bayliss T. 1999 The Rayleigh-like collapse of a conical bubble: Measurements of meniscus, liquid pressure, and electrochemistry. Berlin. Proceedings of the 137th Meeting of the Acoustical Society of America and the 2nd Convention of the European Acoustics Association (Forum Acusticum 99, integrating the 25th German Acoustics DAGA Conference).

[34] Leighton TG, Cox BT, Phelps AD. 2000 The Rayleigh-like collapse of a conical bubble. *The Journal of the Acoustical Society of America* **107**, 130–142.

[35] Symons DD. 2004 Inertial liquid loading on the nozzle of a needle-free injection device. *Proceedings of the Institution of Mechanical Engineers, Part C: Journal of Mechanical Engineering Science* **218**, 233–240.

[36] Bergmann R, De Jong E, Choimet JB, Van der Meer D, Lohse D. 2008 The origin of the tubular jet. *Journal of Fluid Mechanics* **600**, 19–43.

[37] Tagawa Y, Oudalov N, Ghalbzouri AE, Sun C, Lohse D. 2013 Needle-free injection into skin and soft matter with highly focused microjets. *Lab Chip* **13**, 1357–1363.

[38] Tagawa Y, Yamamoto S, Hayasaka K, Kameda M. 2016 On pressure impulse of a laser-induced underwater shock wave. *Journal of Fluid Mechanics* **808**, 5–18.

[39] Morsink G. 2011 Tubular jet generation by pressure pulse impact. Master thesis University of Twente.

[40] Avila G, Roberto S, Song C, Ohi CD. 2015 Fast transient microjets induced by hemispherical cavitation bubbles. *Journal of Fluid Mechanics* **767**, 31–51.

[41] Arora A, Hakim I, Baxter J, Rathnasingham R, Srinivasan R, Fletcher DA, Mitragotri S. 2007 Needle-free delivery of macromolecules across the skin by nanoliter-volume pulsed microjets. *Proceedings of the National Academy of Sciences* **104**, 4255–4260.

[42] Kiyama A, Tagawa Y, Ando K, Kameda M. 2016 Effects of a water hammer and cavitation on jet formation in a test tube. *Journal of Fluid Mechanics* **787**, 224–236.

[43] Ory E, Yuan H, Prosperetti A, Popinet S, Zaleski S. 2000 Growth and collapse of a vapor bubble in a narrow tube. *Physics of Fluids* **12**, 1268–1277.

[44] Giavedoni MD, Saita FA. 1999 The rear meniscus of a long bubble steadily displacing a Newtonian liquid in a capillary tube. *Physics of Fluids* **11**, 786–794.

[45] López-Villa A, Medina A, Higuera FJ. 2011 Bubble growth by injection of gas into viscous liquids in cylindrical and conical tubes. *Physics of Fluids* **23**, 102102.

[46] Duchemin L, Popinet S, Josserand C, Zaleski S. 2002 Jet formation in bubbles bursting at a free surface. *Physics of Fluids* **14**, 3000–3008.

[47] Blake JR, Hooton MC, Robinson PB, Tong RP. 1997 Collapsing cavities, toroidal bubbles and jet impact. *Philosophical Transactions of the Royal Society of London A: Mathematical, Physical and Engineering Sciences* **355**, 537–550.

[48] Turangan CK, Jamaluddin AR, Ball GJ, Leighton TG. 2008 Free-Lagrange simulations of the expansion and jetting collapse of air bubbles in water. *Journal of Fluid Mechanics* **598**, 1–25.

[49] Jamaluddin AR, Ball GJ, Turangan CK, Leighton T. 2011 The collapse of single bubbles and approximation of the far-field acoustic emissions for cavitation induced by shock wave lithotripsy. *Journal of Fluid Mechanics* **677**, 305–341.

[50] Turangan CK, Ball GJ, Jamaluddin AR, Leighton TG. 2017 Numerical studies of cavitation erosion on an elastic–plastic material caused by shock-induced bubble collapse. *Proceedings of the Royal Society of London A: Mathematical, Physical and Engineering Sciences* **473**.

[51] Chandra N, Ganpule S, Kleinschmit NN, Feng R, Holmberg AD, Sundaramurthy A, Selvan V, Alai A. 2012 Evolution of blast wave profiles in simulated air blasts: experiment and computational modeling. *Shock Waves* **22**, 403–415.

[52] Ball GJ. 1996 A Free-Lagrange method for unsteady compressible flow: simulation of a confined cylindrical blast wave. *Shock Waves* **5**, 311–325.

[53] Greenshields C. 2015 *OpenFOAM - The Open Source CFD Toolbox - User Guide*. OpenFOAM Foundation Ltd. 2.4.0 edition.

[54] Kyriazis N, Koukouvinis P, Gavaises M. 2018 Modelling cavitation during drop impact on solid surfaces. *Advances in Colloid and Interface Science* **260**, 46 – 64.

[55] Örley F, Trummler T, Hickel S, Mihatsch MS, Schmidt SJ, Adams NA. 2015 Large-eddy simulation of cavitating nozzle flow and primary jet break-up. *Physics of Fluids* **27**, 086101.

[56] van der Heul DR, Vuik C, Wesseling P. 2000 Efficient computation of flow with cavitation by compressible Pressure Correction. Barcelona. ECCOMAS.

[57] Toro EF. 2009 *Riemann Solvers and Numerical Methods for Fluid Dynamics, A Practical Introduction*. Springer Berlin Heidelberg.

[58] Schmidt S, Sezal I, Schnerr G, Talhamer M. 2008 Riemann Techniques for the Simulation of Compressible Liquid Flows with Phase-Transition at all Mach Numbers - Shock

and Wave Dynamics in Cavitating 3-D Micro and Macro Systems. 46th AIAA Aerospace Sciences Meeting and Exhibit Reno, Nevada. AIAA.

[59] Dear JP, Field JE. 1988 A study of the collapse of arrays of cavities. *Journal of Fluid Mechanics* **190**, 409–425.

[60] Kodama T, Tomita Y. 2000 Cavitation bubble behavior and bubble–shock wave interaction near a gelatin surface as a study of in vivo bubble dynamics. *Applied Physics B* **70**, 139–149.

[61] Edwards C, Marks R. 1995 Evaluation of biomechanical properties of human skin. *Clinics in Dermatology* **13**, 375–380.